

# NUMERICAL ANALYSIS OF THIN-WALLED STRUCTURES IN HYPERSONIC FLOW REGIME

**Matthias C. Haupt, Reinhold Niesner, Ralf Unger, Peter Horst**

**Institute of Aircraft Design and Lightweight Structures**

**Technische Universität Braunschweig**

**Hermann-Blenk-Str. 35, 38108 Braunschweig, Germany**

**e-mail: m.haupt@tu-bs.de, phone: +49-(0)531-3919917, fax: +49-(0)531-3919904**

**Keywords:** *Fluid-Structure Interaction, Aerothermoelasticity, Thermal Buckling, Panel Flutter*

## Abstract

*An approach to couple individual analysis codes is described to investigate fluid-structure interactions. Two applications with thin-walled structures – supersonic panel flutter and aerothermoelastic buckling – demonstrate the applicability of this coupling approach. The supersonic panel flutter is used for validation of highly transient mechanical interactions. The thermal and mechanical interactions including aerothermoelastic buckling is a rarely considered topic.*

## 1 Introduction

For the structural design of launcher and reentry vehicles, minimum weight is an essential requirement. The complex thermal and mechanical loading conditions must be taken into account to reach an optimal structural design. Nowadays, coupled simulations to analyze and to understand the complex fluid-structure interactions become more important, not only for academic but also for industrial applications.

Up to now numerical analyses of thermal and mechanical fluid-structure interactions were done in most case with special software configurations developed for special applications, e.g. see [1], [2] or [3]. In this paper a modular software approach is described, which has been used in a unified way for different types of fluid-structure interactions. It has shown the capability to cou-

ple stand-alone analysis codes for fluid and structure easily. This contribution focuses on thin plate structures subjected to hypersonic fluid flow with application, e.g. to thermal protection systems. Another exemplary application is given for a completely different flight regime in [4] considering flexible airfoils for flapping flight.

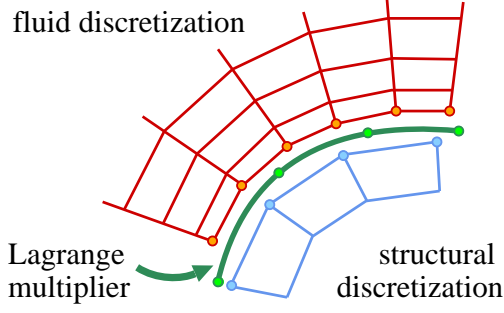
## 2 Simulation approach

In the hypersonic flow regime, the thermal and the mechanical fluid-structure interactions are both important in several applications and must be included into the numerical analyses for an overall understanding. The developed simulation environment uses individually replaceable analysis codes for the fluid and the structural subdomains using the domain decomposition approach and covers both physical couplings.

Within the flexible simulation environment two coupling aspects need to be considered: firstly, the data transfer of the physical coupling values (temperature and deflections) over non-conforming surface discretizations and secondly, the solution of the equilibrium equations and the time integration.

### 2.1 Nonconforming Discretizations

The conservative data exchange between the non-conforming discretizations on the coupling surface  $\Gamma_{fs}$  is based on the weak formulation of the continuity conditions [5], where the jumps of the


**Fig. 1** Grid coupling via Lagrange multipliers

state variables  $\phi$ , i.e. deflections  $u$  and temperatures  $T$ , of the subdomains fluid  ${}^f\Omega$  and structure  ${}^s\Omega$  is weighted by Lagrange multipliers  ${}^\phi\lambda$  (figure 1):

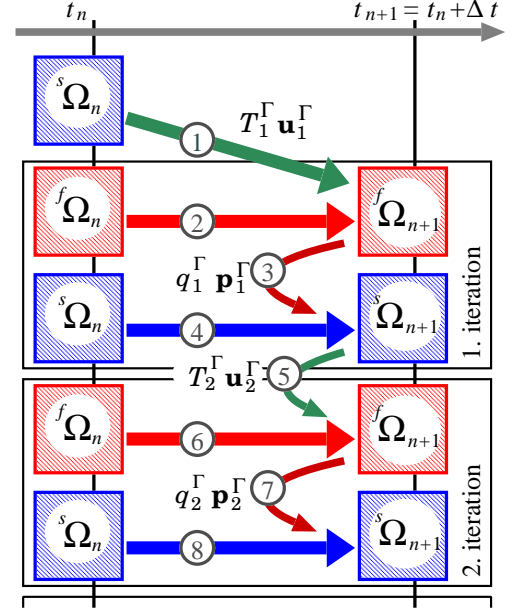
$$\int_{\Gamma_{fs}} {}^u\lambda ({}^s u - {}^f u) d\Gamma, \quad \int_{\Gamma_{fs}} {}^T\lambda ({}^s T - {}^f T) d\Gamma. \quad (1)$$

Using shape functions of the subdomain discretizations and for the Lagrange multipliers, a matrix system  ${}^f\phi|_{\Gamma} = \mathbf{P} \cdot {}^\phi\lambda|_{\Gamma}$  results, which relates the discrete degrees of freedom of both subdomains  ${}^f\phi|_{\Gamma}$  and  ${}^\phi\lambda|_{\Gamma}$  on the coupling surface. It has to be used in its transposed form for the relation between the consistent mechanical and thermal fluxes  ${}^f\phi_{,n}|_{\Gamma}$  and  ${}^\phi\phi_{,n}|_{\Gamma}$  due to reasons of energy conservation:  ${}^f\phi_{,n}|_{\Gamma} = \mathbf{P}^T \cdot {}^\phi\phi_{,n}|_{\Gamma}$ .

The Dirac delta functions at the fluid interface nodes are the standard choice for the shape functions of the Lagrange multiplier, resulting in the simple interpolations scheme. In case of significant different fluid and structural mesh sizes unphysical artifacts occur especially in the load transfer: High loads are generated at the structural points close to the fluid grid points, which is not applicable to thin structures. Locally more accurate is the use of the fluid shape functions comparable to the Mortar-technique and for 3D configurations, a sophisticated evaluation of the weak transfer condition (1) is required, see [6].

## 2.2 Solution of Coupled Equations

For the solution of the coupled equation set, the classical Dirichlet-Neumann iteration with the Dirichlet problem  $\mathbf{F} {}^f\phi|_{\Gamma} = {}^f\phi_{,n}|_{\Gamma}$  on the fluid side and the Neumann problem on the structural


**Fig. 2** Iteration sequence in a coupling time-step

side  ${}^\phi\phi|_{\Gamma} = \mathbf{S}^{-1} \cdot {}^\phi\phi_{,n}|_{\Gamma}$  and a relaxation of the structural interface state  ${}^\phi\phi|_{\Gamma}$  ( $\phi$ :  $T$  or  $u$ ) from iteration  $i$  to  $i+1$  is applied:

$$\tilde{\phi}_i|_{\Gamma} = \mathbf{S}^{-1} \cdot \mathbf{P}^T \cdot \mathbf{F} \cdot \mathbf{P} \cdot {}^\phi\phi_i|_{\Gamma}, \quad (2)$$

$${}^\phi\phi_{i+1}|_{\Gamma} = \omega \cdot \tilde{\phi}_i|_{\Gamma} + (1 - \omega) \cdot {}^\phi\phi_i|_{\Gamma}. \quad (3)$$

An automatic determination of an optimal relaxation parameter  $\omega$ , which is derived from the Aitken method or the gradient method, is able to accelerate the iteration procedure considerably [7]. The handling of transient coupled simulations is performed using iterative staggered procedures, viz. an equilibrium iteration to advance from time level  $n$  to  $n+1$ . The consistent coupling in time requires the same time dependency of the coupling variables imposed by the time integration schemes of the subdomains. The application of second-order predictors [8] (step 1 in figure 2) is valuable to reduce the number of required coupling iterations. Especially for heating simulations, an automatic time-step control without the need for additional higher-order solutions is helpful to improve efficiency [9].

## 3 Software Environment

Figure 3 shows schematically the developed software architecture. The individual processing

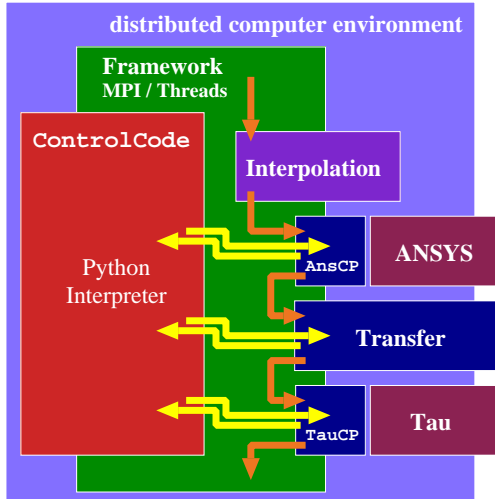


**Fig. 3** Software components for a multidisciplinary simulation

units (solver, interpolation methods, etc.) are defined as operational components in a framework. The components can be considered as separate processes, which can be run on different machines, and can be combined and replaced in a proper way. The several solver codes are adapted to the framework via adapters. In these investigations the finite element code ANSYS is used on the structural side and the DLR-Tau code [10] for the fluid analysis. The sequence of running the components is coordinated by the special ControlCode component, which can be easily programmed in the scripting language Python. The underlying framework provides the mechanisms for communication between the components. Currently two framework implementations are available, which are based on Threads or MPI for communication. The latter one is compatible to the grid coupling library MpCCI.

## 4 Thin-Walled Structures

### 4.1 Supersonic Panel Flutter

The application of the simulation environment to supersonic panel flutter is used for validation of the transient mechanical couplings including additional thermal effects. For this reason the coupled simulations are based on the transient Euler equations of the flow. Only simulation results

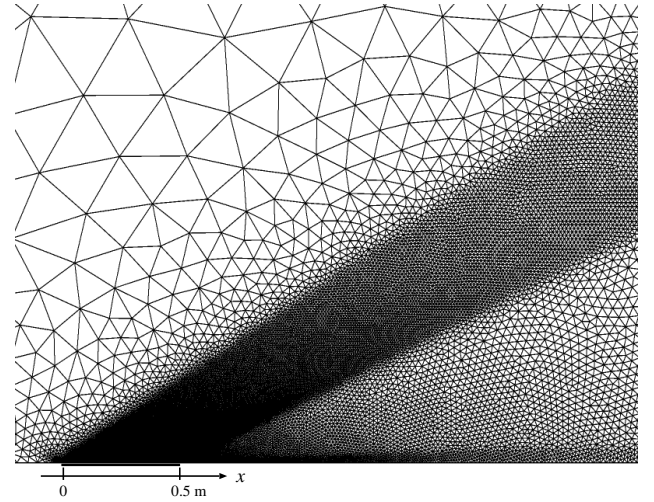


**Fig. 4** Fluid grid and plate configuration

of two dimensional supersonic flutter of a simply supported flat plate are discussed here due to the paper limitations. The mechanical plane strain model utilizes a finite element plate formulation of the nonlinear Reissner-Mindlin theory.

The configuration of the plate and the fluid grid is given in figure 4. The following parameters were selected for the fluid: Mach-number  $M_\infty = 2.0$  and density  $\rho_\infty = 0.448 \text{ kg/m}^3$  and for the structure: plate length  $l = 0.5 \text{ m}$ , thickness  $h = 0.004 \text{ m}$ , E-modulus  $E = 7.3 \cdot 10^{10} \text{ N/m}^2$ , density  $\rho = 2800 \text{ kg/m}^3$  and thermal elongation  $\epsilon_T = 22.610^{-6} \text{ K}^{-1}$ . The critical buckling temperature is  $\Delta T_{crit} = 2.625 \text{ K}$ . The dimensionless mass ratio is in this case  $\mu = \rho l / \rho h = 0.02$ .

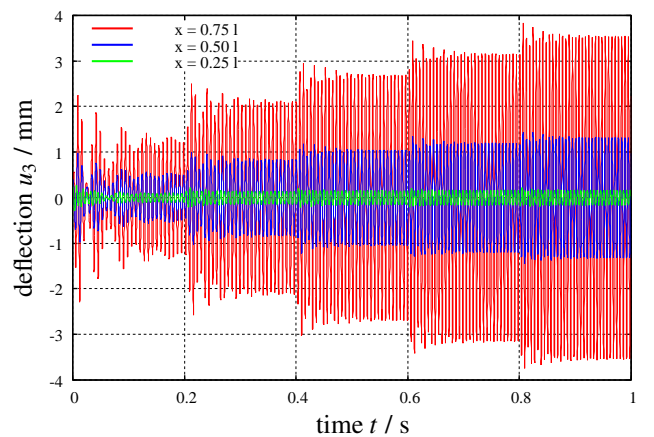


**Fig. 5** Variation 1: deformation histories for a stepped pressure increase

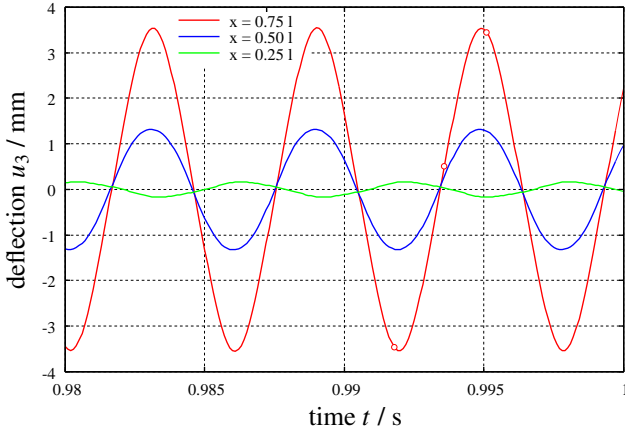


**Fig. 6** Variation 1: deformation history detail at  $f p_\infty = 600 \text{ kPa}$ .

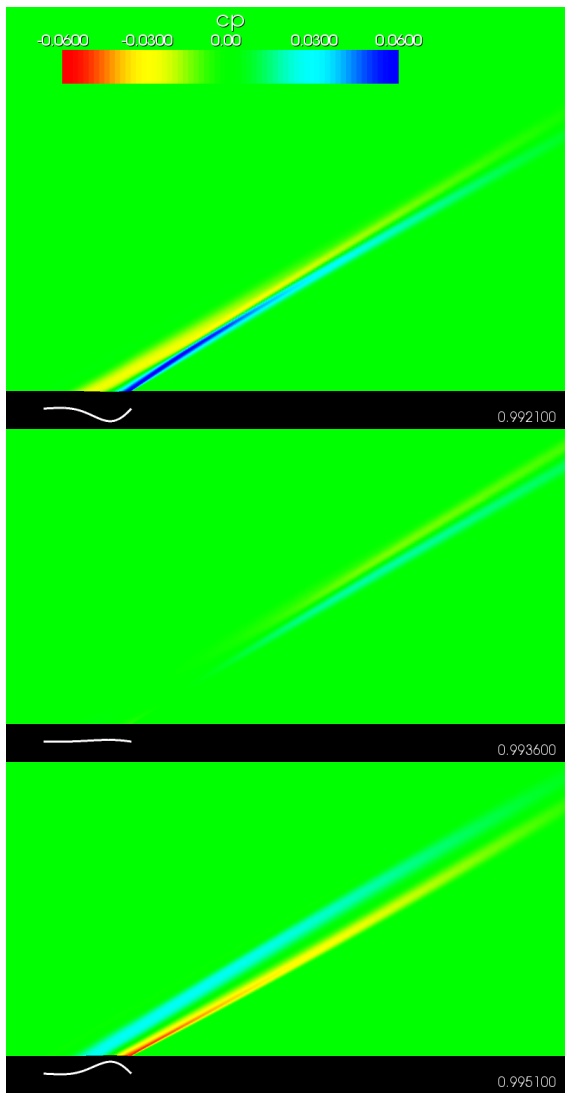


**Fig. 7** Plate deflections (3x amplified) and pressure coefficient  $c_p$  at  $f p_\infty = 600 \text{ kPa}$

Starting from an undeformed state without any thermal stresses and with a small initial vertical velocity based on a sinoidal distribution, the plate oscillates with a limited amplitude at a free stream pressure  $f p_\infty = 400 \text{ kPa}$ .

In variation 1 an increase of the pressure ( $\Delta f p_\infty = 50 \text{ kPa}$  each 0.2 s) provides an increasing amplitude with a maximum at the plate position  $x = 0.75 l$  (figure 5). Due to the nonlinear structural behaviour the plate stiffens during bending due to the membrane forces and the amplitude remains limited and the type of behaviour is a limit cycle oscillation (LCO). For the highest pressure the oscillation is harmonic (figure 6). The mode shape of the plate and the pressure distributions are shown in figure 7.

In variation 2 an additional temperature load  $\Delta^s T$  induces an elongation of the plate and in turn a larger amplitude and a decreased frequency (figure 8). For  $\Delta^s T = 10 \text{ K}$  the oscillation remains harmonic. Due to the additional thermal stresses, the structural behaviour becomes more complex and an additional snap-through at zero-crossing can be observed. As a consequence higher order mode shapes become more active. This non-harmonic behaviour can be seen for  $\Delta^s T \geq 20 \text{ K}$  in figure 8 and 9 and in the deformations of figure 10. For  $\Delta^s T = 50 \text{ K}$  the motion becomes periodic again but is non-sinoidal in the considered time frame.

The results are in very good agreement with the classical solution of [11]. Usual is the repre-

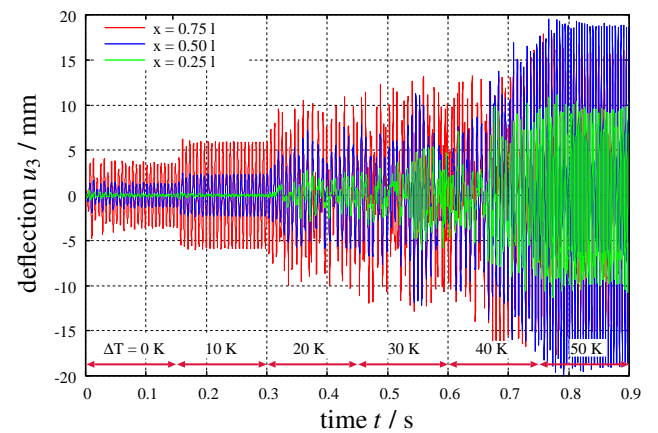


**Fig. 8** Variation 2: deformation histories with stepped temperature increase for  $f p_\infty = 600 \text{ kPa}$

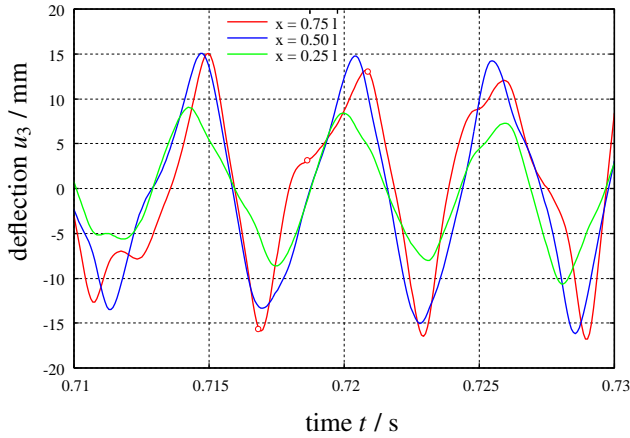


**Fig. 9** Variation 2: deformation history detail with  $\Delta^s T = 40$  K and  $f p_\infty = 600$  kPa

sensation in the diagram (figure 11) with dimensionless dynamic pressure  $\lambda_p$

$$\lambda_p = \frac{f \rho u_\infty^2 12(1 - \nu^2) l^3}{\sqrt{Ma^2 - 1} Eh} \quad (4)$$

plotted versus the plates temperature. Four domains are distinguished:

1. a domain of harmonic LCO,
2. a domain of chaotic oscillations,
3. a domain where the plate remains flat and
4. a domain at low pressure where the plate response is a static buckling state.

The variation 3 at  $\Delta^s T = 10$  K and decreasing pressure passes through three domains (figure 12) and demonstrates the correctness of the simulation based of individual codes and a partitioned coupling approach. The first pressure levels ( $f p_\infty = 400, 300$  kPa) induce LCO. The third level ( $f p_\infty = 200$  kPa) yields a damped oscillation with a final undeformed state. Decreasing the pressure ( $f p_\infty = 100, 50$  kPa) destabilizes the plate state and buckling occurs, which reaches not a stationary state due to the applied small dwell time at the individual pressure levels. The further investigations consider the case of this relative low pressure with a pure bending respectively buckling but includes the time accurate thermal coupling between fluid and structure.

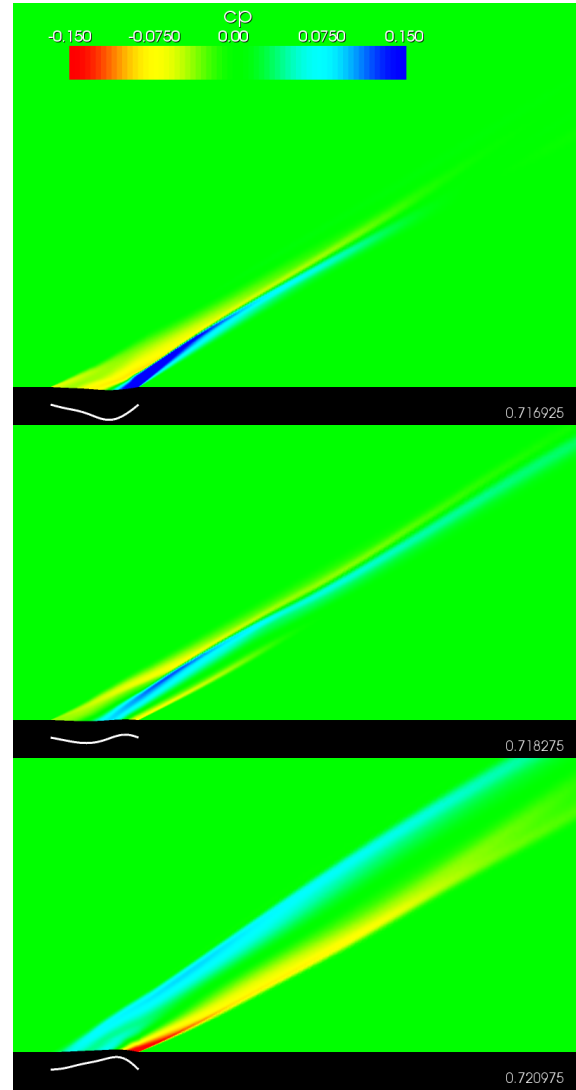


**Fig. 10** Plate deflections (3x amplified) and pressure coefficient  $c_p$  at  $f p_\infty = 600$  kPa and  $\Delta^s T = 40$  K

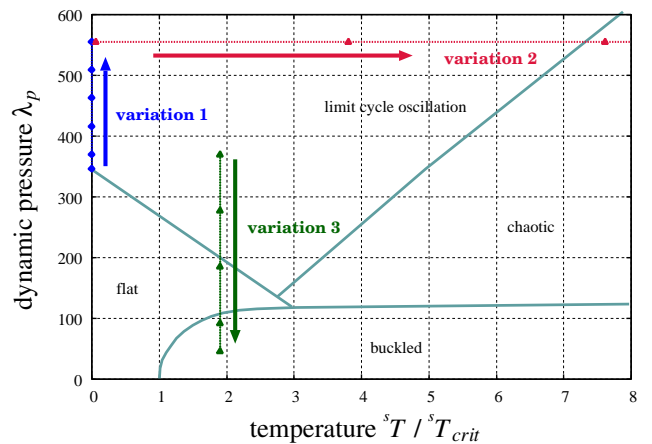


**Fig. 11** Types of structural response

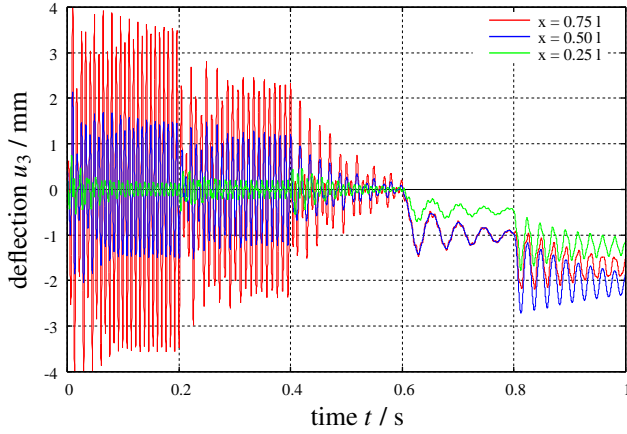


**Fig. 12** Variation 3: deformation histories with  $\Delta^s T = 10\text{K}$  and stepped pressure decrease

## 4.2 Aerothermoelastic Buckling

The following configuration is derived from the work of [12], where metallic plates are considered under uniform and nonuniform temperature distributions. The configuration is subjected here to a hypersonic fluid flow, which heats the plate and induces thermal deformations which in turn influence the flow field. Comparable configurations with thermal-mechanical couplings were investigated rarely, e.g. [13]. Target of this study is the understanding of the complex coupling mechanisms, to design a windtunnel experiment for validation.

The dimensions and the material properties of the Haynes 230 (density  $\rho = 8970 \frac{\text{kg}}{\text{m}^3}$ , emissivity  $\varepsilon_r = 0.8$ , temperature dependent properties see table 1) were adopted to the geometry shown in figure 13 for two dimensions. The clamped plate is supported in a fixed structure with a round leading edge, which induces a detached oblique shock for hypersonic flow conditions. The simulations were started with an undeformed initial state with constant temperature of  $T = 300\text{K}$ . The free stream flow conditions were: angle of attack  $\alpha = 25^\circ$ , Mach number  $M_\infty = 7.27$ , pressure  $p_\infty = 89\text{Pa}$ , density  $\rho_\infty = 4.0210^{-4} \text{kg/m}^3$ , temperature  $T_\infty = 620\text{K}$  and a Reynolds number of  $Re = 8218$  related to the plate length of  $l = 0.1524\text{m}$ . The value of  $358.43 \text{J/kgK}$  is taken for the gas constant  $R$  and  $1.455$  for the isen-

$T$	$E$	$\nu$	$^s c_V$	$^s \varepsilon_T$	$^s \lambda_c$
K	GPa	$\nu$	$\frac{\text{J}}{\text{kgK}}$	$10^{-6}/\text{K}$	$\frac{\text{W}}{\text{mK}}$
294	211	0.310	398	12.6	8.9
478	202	0.315	435	13.0	12.5
700	188	0.321	469	13.7	17.0
922	174	0.330	561	14.6	21.3
1144	159	0.334	607	15.5	25.8
1366	143	0.343	624	16.6	30.3

**Table 1** Properties of the metallic plates [14].

tropic coefficient  $\gamma$ . The coupling is done quasi-stationary with respect to the fluid, where the Navier-Stokes equations are solved, and the mechanical state of the structure and complete transient for their thermal state. The heat transfer between fluid and structure requires a proper resolution of the boundary layer ( $y^+ < 0.5$ ), which makes the fluid simulations more expensive compared with the panel flutter simulations.

### 4.2.1 Metallic plate-stripe

The results of the two-dimensional case and a plate thickness of  $2.3\text{mm}$  show clearly the basic coupling effects and are simple to discuss. Furthermore the effort of parameter studies is significantly lower than in the three-dimensional case. In these analyses of infinite plate-stripes plain strain conditions were assumed.

Due to the aerodynamic heating the temperature of the plate increases and the thermal expansion generates a buckling of the plate at a critical load. The resultant negative deflection is caused by the temperature gradient across the plate thickness and by the aerodynamic pressure pushing the plate slightly downwards (figure 14). But with a small imperfection the plate buckles to the opposite upward direction. Here the first eigenmode with a maximum amplitude of  $0.01$  times the thickness was chosen. The results of both deformation modes are given in figure 15 and 16. In addition, the pure thermal coupled analyses, ignoring the deformation in the fluid analysis, and the results obtained with temperature-dependent material properties and

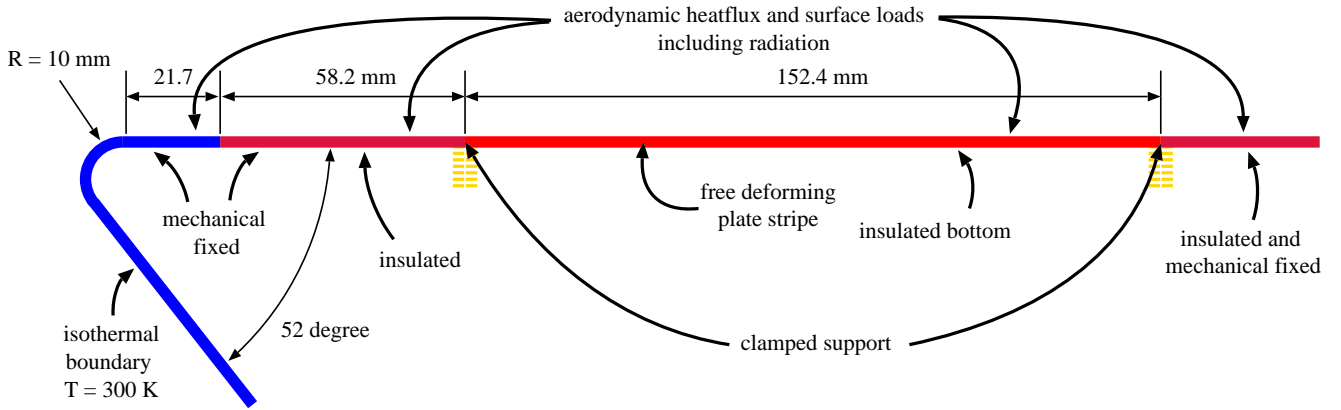


Fig. 13 Geometry and boundary conditions of the two dimensional model

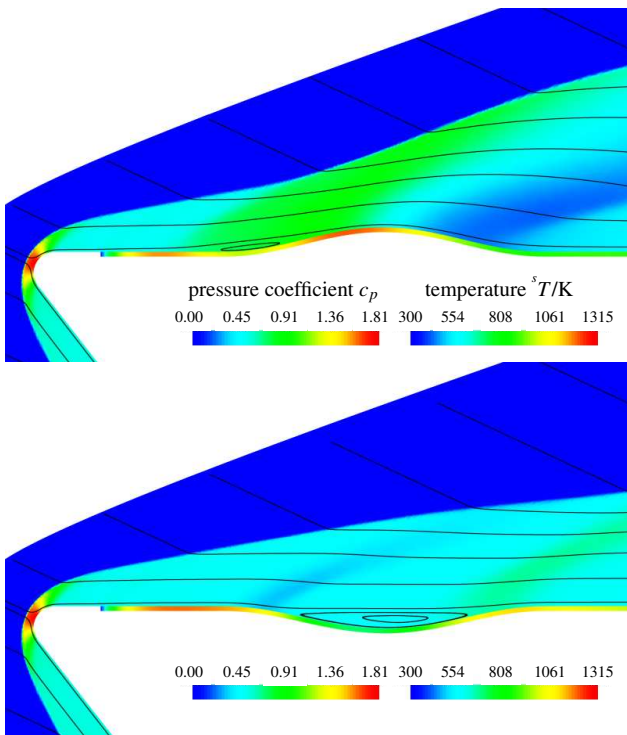


Fig. 14 Streamlines, pressure coefficient  $c_p$  in the flow field and temperature in the plate structure for  $t = 60s$

with constant properties (these of room-temperature) are given.

The average temperature of the plate is higher for the positive buckle resulting in a larger buckling amplitude (figure 16). As to be expected, a positive buckling direction leads to an increase in the plate temperature in comparison to the nondeforming case. In the case of a negative buckle, the temperature increase of the midpoint is signifi-

cantly smaller for times over  $t = 15s$ . The reason is the occurrence of a separation bubble, which reduces the heatflux at the midpoint. The separation bubble can be seen in the corresponding field plot and streamlines of figure 14.

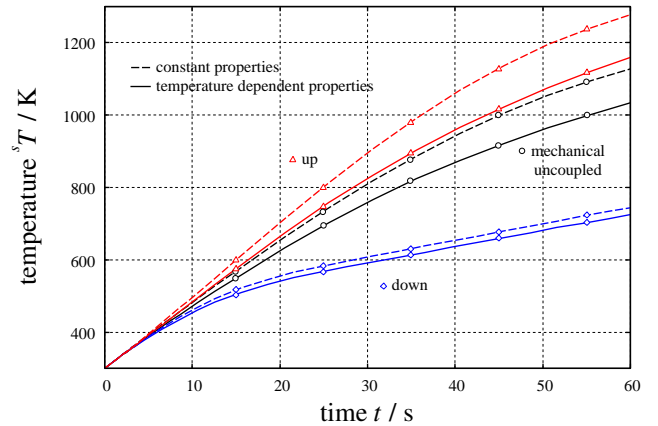
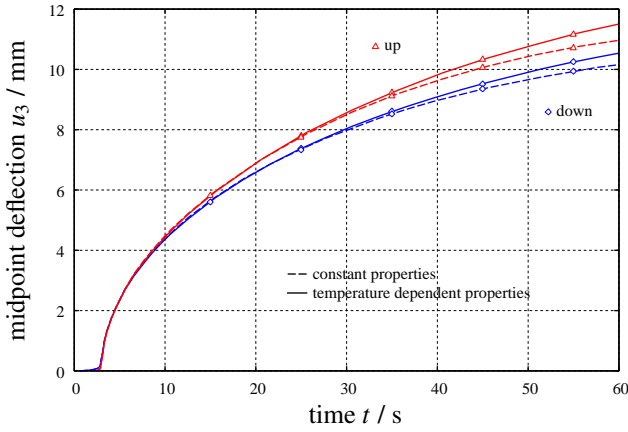


Fig. 15 Temperature histories of the plate midpoint

More revealing are the temperature and heat-flux profiles given in the figure 17. The origin of the coordinate  $x$  matches the plate leading edge. At time  $t = 15s$ , the deformations modulate these profiles around the nondeforming case with opposite sign. At time  $t = 60s$ , the separation bubble reduces the heat flux and temperature in the deforming area. However due to the reattachment of the flow at the downstream clamped support with a stagnation point, a heat load peak induces a temperature increase in comparison with the mechanical uncoupled case. In contrast, the upward buckling leads to a separa-



**Fig. 16** Midpoint deflections (Downward deflection plotted positive for comparison.)

tion bubble in front of and a nearly separation behind the buckle, so that the heat flux and temperature are reduced at these points.

In particular for the upward buckling case the shock-angle alters significantly due to the deformed geometric contour. The change in the downward buckling case is not so strong. To limit the influence of the shock-deformation interaction, the considered time interval is restricted here to 60s. In addition, the maximum temperature reaches a level where the applied simple material law is not valid anymore, because creep or failure are not included.

The differences between temperature-dependent and independent material properties looks important in figure 15. The increase in the heat conduction  $\lambda_c$  with temperature provides lower temperatures than for a constant value. The influence on the buckling amplitude of the midpoint as shown in figure 16 is less important. The deformation modes are in each case in accordance with the buckling mode and therefore not shown in detail. The modulations in the temperature profiles are less significant. The pressure distributions on the plates (figure 17) show a flattening for time  $t = 60s$  indicating a separation bubble. As mentioned before, the pressure for the clamped plate is of minor importance and induces at most an imperfection only important for the buckling direction.

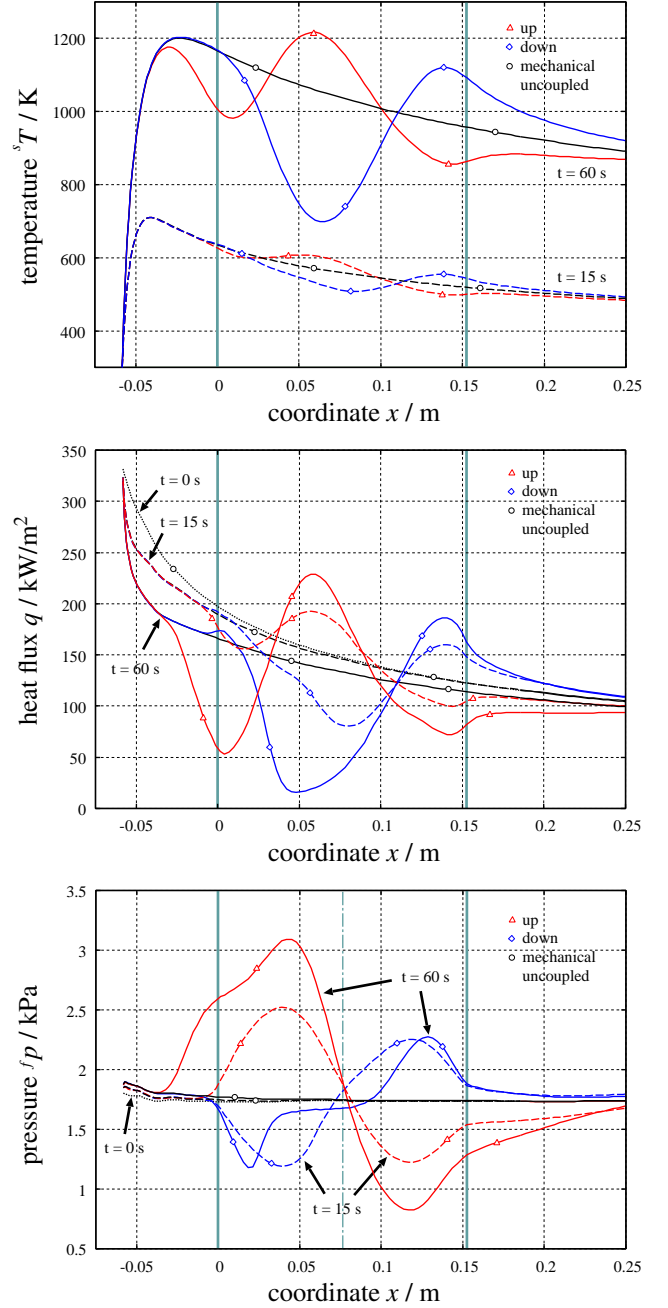


**Fig. 17** Temperature, heat flux and pressure profiles for two time-steps with temperature-dependent material properties

#### 4.2.2 Metallic plate

In the three dimensional analyses only one symmetrical half of the plate is considered as it can be seen in figure 18. The model is extended in the transversal direction to cover one half of the plate with clamped boundary conditions and with an additional nondeforming stripe with a width

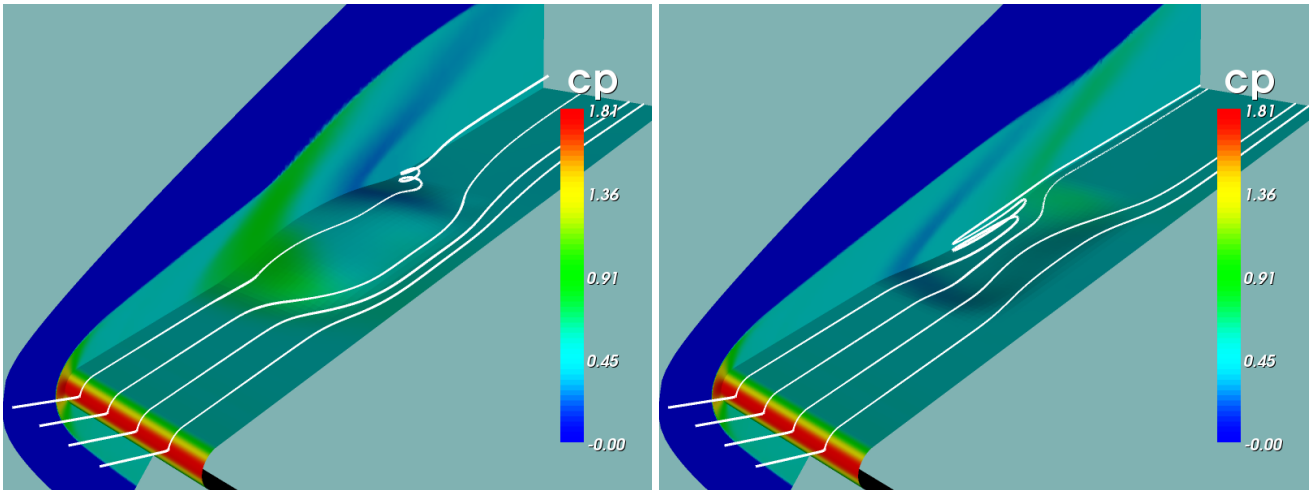


**Fig. 18** Pressure distribution and streamlines for the square plate (152.4x152.4x1.71) buckling upward at  $t = 30$ s and downward at  $t = 20$ s

of 1/10 of the plate width. Symmetry conditions were applied to the fluid grid on both long sides.

The figures show the same basic effects observed in 2D: the buckling of the plate and the separation bubbles. Figure 19 compares the midpoint deflections of the 2D analysis with geometric variations of 3D simulations. Black indicates the plate with the dimensions of 152.4mm×152.4mm×2.3mm, red the same dimensions but a thickness of 1.7mm. This thickness is taken for the green and blue configurations with the dimensions 228.6mm×152.4mm and 228.6mm×228.6mm respectively.

Important observation is the fact that the deformation amplitudes of the plate are in the same order as for the 2D analyses. Although the heating is equivalent the clamped boundary conditions on all sides restrict the bending/buckling deformation. On the other hand these boundary conditions increase the thermal inplane stresses. For this reason the amplitudes are comparable. The thickness decrease shows an earlier buckling and as a consequence a larger amplitude for the thinner plate. The lower heat capacity and bending stiffness are the reasons for this.

Increasing the plate dimension in flow direction a rectangle is considered, which has from the beginning bending ripples near the clamped boundary. At 50s the downward buckling mode switches to a mode with an increased number of

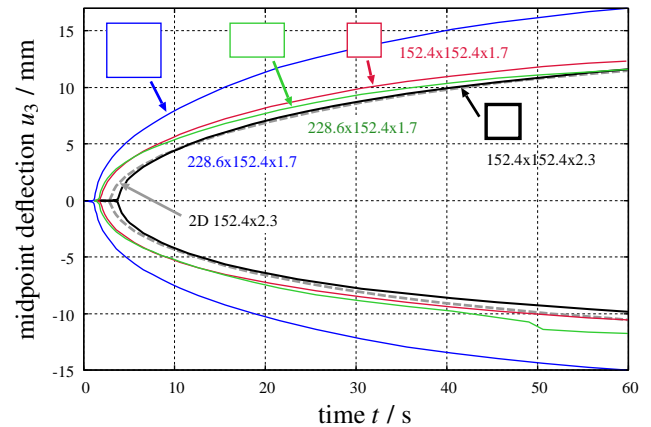


**Fig. 19** Deflections histories for thermal-mechanical coupled analyses.

ripples as it can be seen in figure 20.

Increasing the plate dimension in both dimensions leads to a weaker square plate with significant ripples and larger amplitudes. These ripples occur only in these 3D analyses and are the consequence of the clamped boundary conditions restricting the expansion parallel to the boundary edges. The smaller plate would reach such modes at larger times of heating.

It should be mentioned that the adaptation (shock and boundary layer) and deformation of the fluid grid is one of the key problems performing such simulations. Due to the space limitations this problem can not be discussed here.

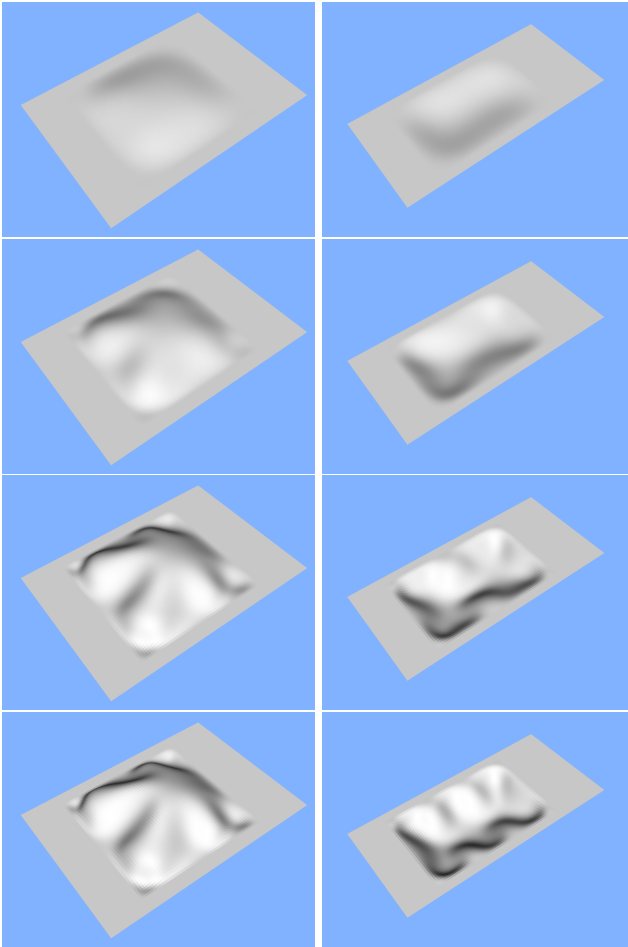


**Fig. 20** Scaled deformations modes for time steps  $t = 5, 15, 40, 60$ s. dimensions left:  $228.6\text{mm} \times 228.6\text{mm}$ , right:  $152.4\text{mm} \times 228.6\text{mm}$

## 5 Acknowledgement

The partial funding of this research under contract 50JR0504 of the Federal Ministry of Economics and Technology through the German Aerospace Center is gratefully acknowledged.

## References

- [1] Liu QY, Luke EA, Cinella P. Coupling heat transfer and fluid flow solvers for multidisciplinary simulations. *J. of Thermophysics and Heat Transfer*. Vol 19(4), pp.417-427, 2005.
- [2] Löhner R, Cebal L., Yang C, Baum JD, Mestreau EL, Charman C, Pelessone D. Large-scale fluid-structure interaction simulations. *Computing in Science and Engineering*, May/June, pp. 27-37, 2004
- [3] Jiao X, Zheng G, Lawlor OS, Alexander PJ, Campbell MT, Heath MT, Fiedler RA. An integration framework for simulations of solid rocket motors. *AIAA-Paper 2005-3991*, 2005.
- [4] Unger R, Haupt MC, Horst P, Windte J. Structural design and aeroelastic analysis of an oscillating airfoil for flapping wing propulsion. *AIAA-Paper 2008-306*, 2008.
- [5] Park K.C., Felippa C.: A Variational Principle for the Formulations of Partitioned Structural Systems. *Int. J. Numer. Meth. Engng.*, 47, 395–418, 2000.
- [6] Unger R, Haupt MC, Horst P. Application of Lagrange Multipliers for Coupled Problems in Fluid and Structural Interactions. *Computers & Structures*, Vol. 85, pp. 796–809, 2007.
- [7] Niesner R, Haupt MC, Horst P. Transient analysis methods for hypersonic applications with thermo-mechanical fluid-structure interactions. *Proc. of 3th ECCOMAS Conference*, Lisbon, Portugal, 2006.
- [8] Piperno S. Explicit/implicit fluid/structure staggered procedures with a structural predictor and fluid subcycling for 2D inviscid aeroelastic simulations. *Int. J. Num. Meth. Fluids*, Vol. 25, pp. 1207–1226, 1997.
- [9] Haupt MC, Niesner R, Unger R, Horst P. Computational Aero-Structural Coupling for Hypersonic Applications. *AIAA-Paper 2006-3252*, 2006.
- [10] Gerhold T, Galle M, Friedrich O, Evans J. Calculations of complex three-dimensional configurations employing the DLR-Tau-Code. *AIAA-Paper 97-0167*, 1997.
- [11] Dowell EH. Nonlinear oscillations of a fluttering plate I. *AIAA Journal*, Vol. 4, pp. 1267–1275, 1966.
- [12] Ko WL. Thermal buckling analysis of rectangular panels subjected to humped temperature Heating. *NASA Technical Report NASA/TP-2004-212041*, 2004.
- [13] Thornton EA. Thermal structures and materials for high-speed flight. *Progress in Astronautica and Aeronautica*, Vol. 140, AIAA, 1992.
- [14] Haynes International Inc. HAYNES 230 alloy. *Product brochure*, 2004.

## 6 Copyright Statement

The authors confirm that they, and/or their company or institution, hold copyright on all of the original material included in their paper. They also confirm they have obtained permission, from the copyright holder of any third party material included in their paper, to publish it as part of their paper. The authors grant full permission for the publication and distribution of their paper as part of the ICAS2008 proceedings or as individual off-prints from the proceedings.